ACS OMEGA

http://pubs.acs.org/journal/acsodf

Article

Cannabidiol-Mediated Green Synthesis, Characterization, and Cytotoxicity of Metal Nanoparticles in Human Keratinocyte Cells

Andrea Jess Josiah, Sreejarani K. Pillai, Werner Cordier, Margo Nell, Danielle Twilley, Namrita Lall, and Suprakas Sinha Ray*

Cite This: *ACS Omega* 2021, 6, 29078−29090

Read Online

ACCESS | Metrics & More | Article Recommendations

ABSTRACT: This study investigated a unique one-pot microwave-assisted green synthesis method of gold (Au) and silver (Ag) nanoparticles (NPs) using cannabidiol (CBD) as a capping and reducing agent. Furthermore, Au and Ag NPs were also chemically synthesized using poly(vinyl pyrrolidone), which functioned as reference materials when comparing the size, shape, and cytotoxicity of NPs. Synthesis parameters such as reaction time, temperature, and precursor molar ratio were optimized to control the size and shape of the biosynthesized NPs. Various characterization techniques such as transmission electron microscopy, ultraviolet−visible spectroscopy, Fourier transform infrared spectroscopy, and X-ray diffraction were used to confirm the formation and properties of Au and Ag NPs. Both biosynthesized metal NPs were spherical and monodispersed, with average particle sizes of 8.4 nm (Au-CBD) and 4.8 nm (Ag-CBD). This study also explored the potential cytotoxicity of CBD-capped NPs in human keratinocyte cells, which was observed to be of minimal concern. The novel synthesis approach presented in this study is free from harsh chemical reagents; therefore, these NPs can be used in a wide array of applications, including the pharmaceutical and biomedical fields.

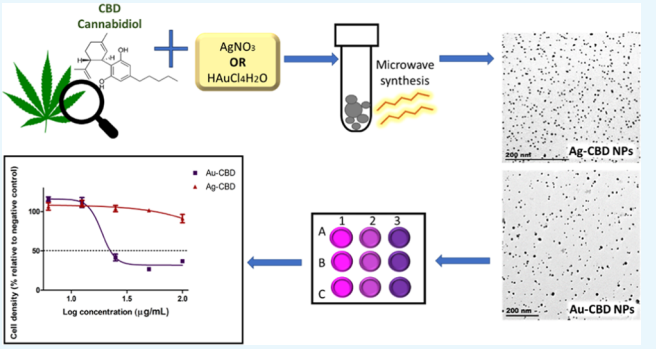

1. INTRODUCTION

Nanotechnology can be defined as a revolutionary research field, which is fundamentally based on the concept of manipulating matter at an atomic level.[1,2] Nanoparticles (NPs) are described as particles with at least one of their dimensions equaling less than 100 nm and only exist in the following two forms: amorphous and crystalline.[3] The behavior of NPs is influenced by surface effects and quantum effects, which alter the chemical reactivity and optical, mechanical, magnetic, and electrical properties.[4] The change in NP properties results in NPs offering a plethora of advantages when compared to bulk materials, particularly increased surface area, enhanced reactivity, lower binding energy linked to decreasing particle size, reduced melting point, and the effects of quantum confinement that results in magnetic moments in NPs.[3] The above-mentioned advantages of NPs are partially why NPs have a wide array of applications in disciplines such as electronics,[5] telecommunication,[6] pollution remediation,[7] cosmetics,[8] and the biomedical field—imaging,[9] tissue engineering/nanoscaffolding,[10] and drug delivery.[11]

The largest and most peripheral organ of the body is the skin, with a surface area in the range of 1.8−2 m^2. The main function of the skin is homeostasis maintenance such as temperature control and protection against thermal, physical, chemical, and biological stressors.[12] The skin can be divided into the following three fundamental layers: epidermis, dermis, and hypodermis[13] (Figure 1).[14] The epidermis is the outermost layer of the skin, acting as a protective barrier against infectious, environmental pathogens.[15] The epidermis is composed of stratified squamous epithelium, which varies in thickness from 7 to 120 μm. It is subdivided into the following five layers: stratum basale, stratum spinosum, stratum granulosum, stratum lucidum, and stratum corneum.[16] The stratum corneum represents the skin's primary anatomical barrier and is approximately 10−20 μm thick. The core function of the stratum corneum is to regulate chemical, drug, and particle absorption into the skin. The dermis is located directly below the epidermis and can be described as the most extensive skin layer. The dermis interacts through the dermal−epidermal junction, and its primary function is the administration of resilience and elasticity to the skin.[15] The hypodermis is also referred to as subcutaneous tissue. It is

Received: August 10, 2021
Accepted: September 24, 2021
Published: October 21, 2021

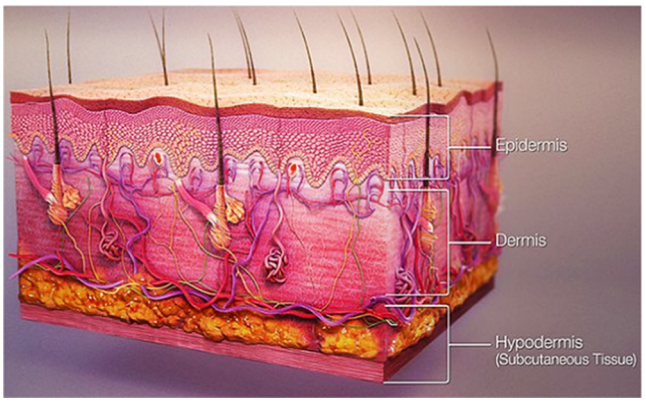

Figure 1. Diagrammatic illustration of three fundamental skin layers. This image is licensed under the Creative Commons Attribution-Share Alike 4.0 International license (https://creativecommons.org/licenses/by-sa/4.0/deed.en), (https://commons.wikimedia.org/wiki/File:3D_medical_animation_skin_layers.jpg,[14] accessed 2021-08-02).

constituted of fatty tissue, and the main functions include physical shock absorption, fat storage, and thermoregulation of the body.[17]

Due to the large surface area and accessibility of the skin, extensive investigations of transdermal drug delivery have been conducted. Transdermal drug administration results in either the drug compound being confined within the skin (topical application) or penetrating the skin to reach the blood circulatory system (transdermal delivery).[18] Several advantages are associated with transdermal drug delivery when compared to conventional drug administration routes, including noninvasiveness, which increases patient compliance, enhanced drug bioavailability, cost effectiveness, and decreased drug plasma concentration fluctuation.[18] Desmet et al.[19] reported that NP-based delivery systems provide improved benefits when treating skin disorders transdermally. These systems reduce the toxic effects related to gastrointestinal complications or systemic absorption.[19] Gupta et al.[20] further explained that NP-based delivery systems are able to implement a controlled release of bioactive compounds, which results in enhanced drug permeation, establish and secure a direct connection with the stratum corneum, and safeguard the drug against physical and chemical instability.[20] Administration of drugs through the skin can follow two potential routes: transepidermal and transappendageal. The transepidermal pathway allows molecules to pass through the stratum corneum and can be further subdivided into intracellular and intercellular pathways.[21] The intracellular route depicts a pathway that permits the transport of hydrophilic or polar solutes through differentiated keratinocytes known as corneocytes.[21]

In contrast, the intercellular route allows the transport of lipophilic or nonpolar solutes via intercellular spaces in the lipid matrix. The second transdermal drug route (transappendageal route) represents a pathway that allows the permeation of molecules via hair follicles that are associated with sebaceous glands and sweat glands.[21] This route is suitable for ions and large polar molecules that experience stratum corneum permeation difficulty.[22] A study by Palmer and DeLouise[23] indicated that NPs prefer utilizing the hair follicle and intercellular pathways to achieve transdermal drug permeation. Several physiochemical NP properties influence its transdermal penetration, such as shape, charge, chemical composition, size, surface area, and stability. In addition, the skin's physical state is a contributing factor to the transdermal absorption of NPs. Niska et al.[24] demonstrated the relationship between NP size and penetration and permeation in normal and damaged skin (Table 1).

Table 1. Effect of Nanoparticle Size on Skin Penetration and Permeation

	penetration and permeation	
nanoparticle size (nm)	normal skin	damaged/abnormal skin
≤4	yes	[a]NE
4−20	yes	yes
21−45	NE	yes
>45	NE	NE

[a]NE, Not exhibited.

A study by Salber et al.[25] reported that the increased surface area exhibited by gold (Au) NPs enhanced keratinocyte cell adhesion and proliferation and, therefore, can potentially be employed in skin tissue engineering applications. Gupta and Rai[26] reported on the transdermal permeation of dodecanethiol-coated AuNPs (2−5 nm) using molecular dynamics simulations. The study demonstrated that electrically neutral AuNPs are capable of infiltrating the skin lipid bilayer, resulting in structural changes and the formation of cavities within the interior of the bilayer. Electrically charged AuNPs were unable to penetrate the lipid bilayer but were absorbed on the surface. Therefore, AuNPs can be used in targeted drug delivery systems.[26] Tian et al.[27] showed that topical application of silver (Ag) NPs increased the rate of wound healing by inhibiting bacterial activity and minimizing inflammation. Another study revealed that AgNPs (10−50 nm) function as skin cells protective shield against DNA damage, DNA mutation, and apoptosis, caused by ultraviolet B (UVB) radiation.[28]

NP synthesis can occur via chemical, physical, and green/biosynthesis. Both chemically and physically synthesized NPs contain key features that have been positively altered for applications in diverse research fields,[29] as mentioned above. However, many disadvantages are closely linked to these methods, such as lengthy labor-intensive processes, high energy, elevated cost, the use of nonbiocompatible chemicals as reducing and capping agents, and generation of toxic effects that have negative impacts on the environment.[30] Due to the above-mentioned challenges, green synthesis of NPs has attracted growing interest in various research fields, owing to the multitude of advantages they offer, such as biologically nontoxic reagents, using environmentally friendly capping and reducing agents, low-energy and cost-effective processes, one-step synthesis process, and greater stability of NPs produced.[31] Plant extracts are composed of phytochemicals that provide ideal capping, reducing, and stabilizing properties required for metal NP (MNP) synthesis.[32] Shafey[33] explained that phytochemicals target metal-ion reduction, which results in NP formation. Previous literature has shown that the essential phytochemicals accountable for the synthesis of NPs include phenols, terpenoids, flavones, ketones, aldehydes, amides, and carboxylic acids.[32] Green synthesis of MNPs follows a sequential three-step procedure: activation, growth, and process termination. The activation step involves metal-ion reduction, which results in creating new structures that comprise reduced metal ions by nucleation (self-organization). The second step includes further reduction of metal ions and the growth of newly formed

https://doi.org/10.1021/acsomega.1c04303
ACS Omega 2021, 6, 29078−29090

metal-ion structures. The last step of process termination is vital for NP synthesis, as it is responsible for the shape and stability of NPs.[34]

A major drawback associated with plant extracts employed in phytotherapy is the inadequate control and standardization of extracts. Several factors influence the quantity and quality of bioactive components contained within a plant extract, such as climate, plant genetics, soil quality, time of harvest, and method of extraction.[35] The poor standardization of plant extracts results in irreproducible NP synthesis and inconsistent NP biological activity. However, the use of isolated plant bioactive compounds can circumvent these challenges and are preferred in biogenic NP synthesis.

Cannabidiol (Figure 2)[36] (CBD; IUPAC name, 2-[(1R,6R)-3-methyl-6-(prop-1-en-2-yl)cyclohex-2-en-1-yl]-5-pentylbenzene-1,3-diol) is a prominent nonpsychoactive phytocannabinoid in the *Cannabis* flowering plant, which is a member of the Cannabaceae family.[37] The hallmark of CBD is its nonpsychoactivity and the absence of biological activity on body temperature and motor function.[38] These key features create an attractive natural compound that lends itself to an array of therapeutic applications in the medical field, such as the topical application of CBD in treating certain skin disorders, including atopic dermatitis,[39] epidermolysis bullosa,[40] and acne/seborrhea.[41] Cannabidiol is a 21-carbon terpenophenolic compound.[42] Phenolic compounds consist of one or more aromatic rings that contain at least one hydroxyl group.[43] Phenolic compounds can be employed as reducing agents in NP synthesis, where the bioreduction ability of the phenolic compound is dependent on the number of functional hydroxyl groups.[33] Other research groups explain that a bond is formed between the carboxyl group in a phenolic compound and the metal atom, which leads to the phenolic compound being absorbed onto the NP surface.[44,45] This phenomenon results in phenolic compound-capped NPs that demonstrate enhanced stability when compared to other reducing agents.[46]

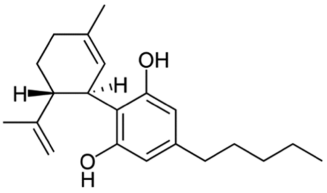

Figure 2. Chemical structure of cannabidiol. This image is licensed under the Creative Commons Attribution-Share Alike 3.0 unported license (https://creativecommons.org/licenses/by-sa/3.0/deed.en), (https://commons.wikimedia.org/wiki/File:Cannabidiol.png),[36] accessed (2021-09-10).

In this study, a microwave-assisted hydrothermal process was employed for NP synthesis, primarily due to its energy efficiency. Additionally, there are several advantages that microwave-assisted synthesis offers when compared to conventional synthesis, including increased yield and purity of particles, time and cost efficiency, uniform and rapid heating of materials, and narrow particle size distribution of NPs.[47] Furthermore, our research group previously reported the synthesis of AgNPs by a microwave-assisted method where no reducing agents were employed.[48]

According to the authors' knowledge, there have been no scientific reports on the use of CBD in green synthesis or the cytotoxicity of CBD-capped NPs in human keratinocytes. This study investigated (i) the potential of CBD to function as an environmentally friendly capping and reducing agent in MNP synthesis and (ii) comparative cytotoxicity analysis of CBD and CBD-capped NPs in keratinocyte (HaCaT) cells.

2. RESULTS AND DISCUSSION

2.1. NP Formation. NPs were synthesized via the following two routes: (i) a chemical route using PVP, a nontoxic biopolymer, which functioned as a capping agent,[49] and (ii) a biogenic route using CBD, a phytocannabinoid, which functioned as a capping and reducing agent.[42] Koczkur et al.[50] described PVP as an excellent stabilizing agent that prevents NP agglomeration, and Chang et al.[51] reported that PVP serves as a reducing agent in the formation of noble metal NPs. The primary mechanism for the influence of PVP on NPs is the steric hindrance effect, which can be explained by hydrophobic carbon chains that are present in PVP, which infiltrate solvents and subsequently generate molecular interactions, giving rise to repulsive forces.[50] Studies have reported on secondary metabolites of plants, such as phenolic compounds, flavonoids, alkaloids, and terpenoids, that are capable of reducing metal ions into corresponding NPs.[52] Singh et al.[53] explored an aqueous stem extract from *C. sativa*as capping and reducing agents for the formation of AgNPs and AuNPs.[53] However, there have been no studies to date, to the author's knowledge, that have investigated the potential capping and reducing abilities of the CBD isolate for NP synthesis. Therefore, to correlate the analysis of CBD-capped NPs to the previous literature, characterization results will be compared to studies that involve phenolic compounds or terpenes as a capping and reducing agent in NP synthesis. This is aimed at providing a partial validation of the characterization results. Tables 2 and 3 provide the optimal conditions that were employed in chemical and biogenic NP syntheses.

The synthesis of AgNPs yielded the following two different color changes: (i) colorless to dark yellow when using PVP and (ii) colorless to light gray when using CBD. The color change represents a chemical reduction reaction, where Ag^+ ions are reduced to Ag^0, and also demonstrates the formation of AgNPs.[54] The TEM images corresponding to Ag-PVP NPs (Figure 3a) and Ag-CBD NPs (Figure 3d) both display spherical, monodispersed AgNPs. However, Ag-PVP NPs vary in size, when compared to Ag-CBD NPs, which are uniformly sized.

Furthermore, the TEM images show that the particles are not aggregated due to the effective capping efficiency of PVP and CBD. The capping on AgNPs is not visible from the TEM image, which indicates that the capping agent concentration used was

Table 2. Optimized Parameters Implemented in Chemical Nanoparticle Synthesis

nanoparticles	PVP[a] (g)	concentration of precursor salt (M)	volume of precursor salt (mL)	synthesis time (min)	synthesis temperature (°C)
Silver	0.5	0.1	1	10	100
Gold	0.5	0.1	2	30	100

[a]Polyvinylpyrrolidone.

https://doi.org/10.1021/acsomega.1c04303
ACS Omega 2021, 6, 29078−29090

Table 3. Optimized Parameters Implemented in Biogenic Nanoparticle Synthesis

NPs	concentration of CBD[a] (M)	volume of CBD (mL)	concentration of precursor salt (M)	volume of precursor salt (mL)	synthesis time (min)	synthesis temperature (°C)
Silver	0.00025	25	0.1	1	10	100
Gold	0.00025	25	0.1	1	20	100

[a]Cannabidiol.

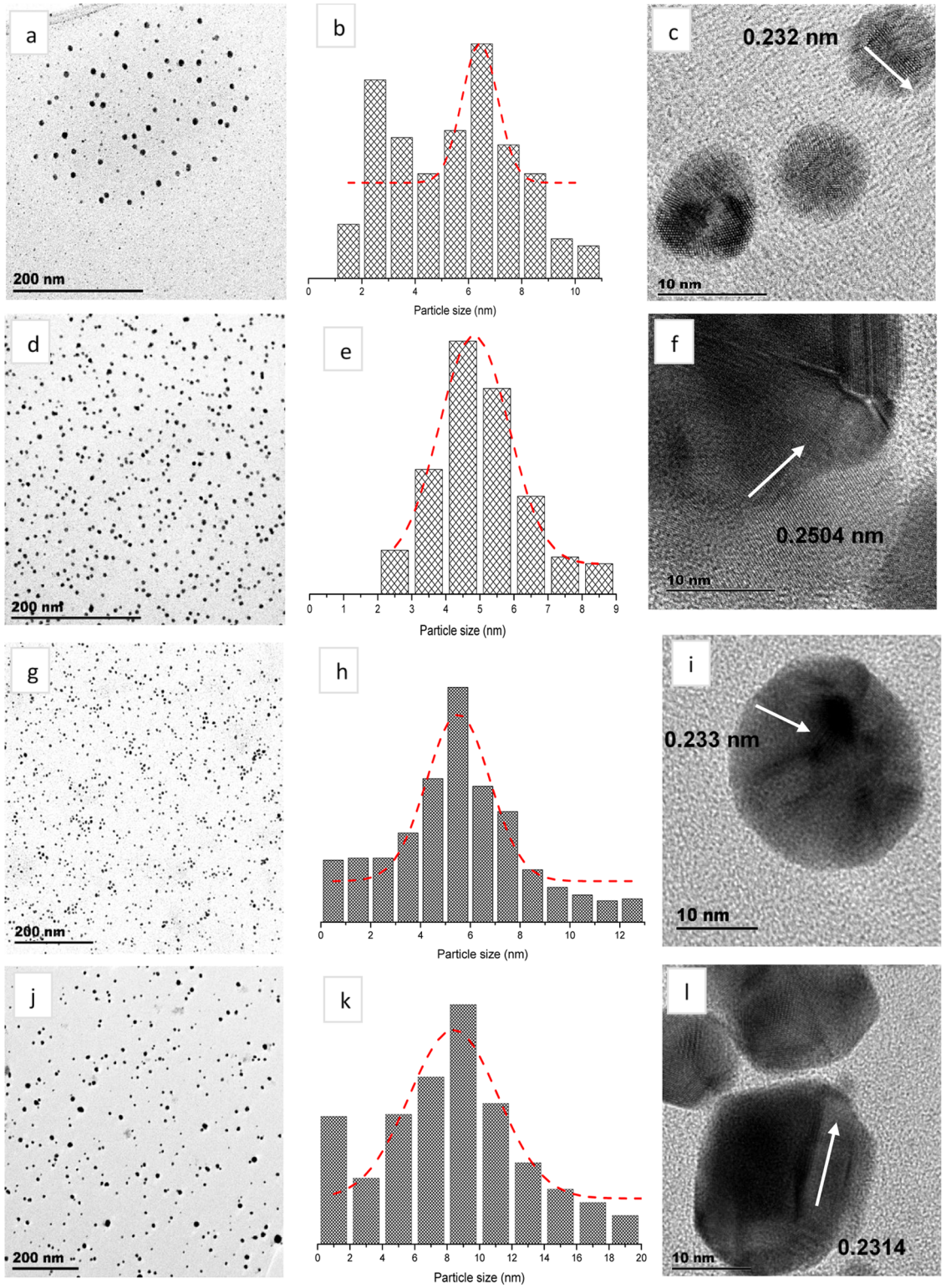

Figure 3. Morphology and size analyses of NPs. (a–c) PVP-capped AgNPs, (d–f) CBD-capped AgNPs, (g–i) PVP-capped AuNPs, and (j–l) CBD-capped AuNPs.

https://doi.org/10.1021/acsomega.1c04303
ACS Omega 2021, 6, 29078−29090

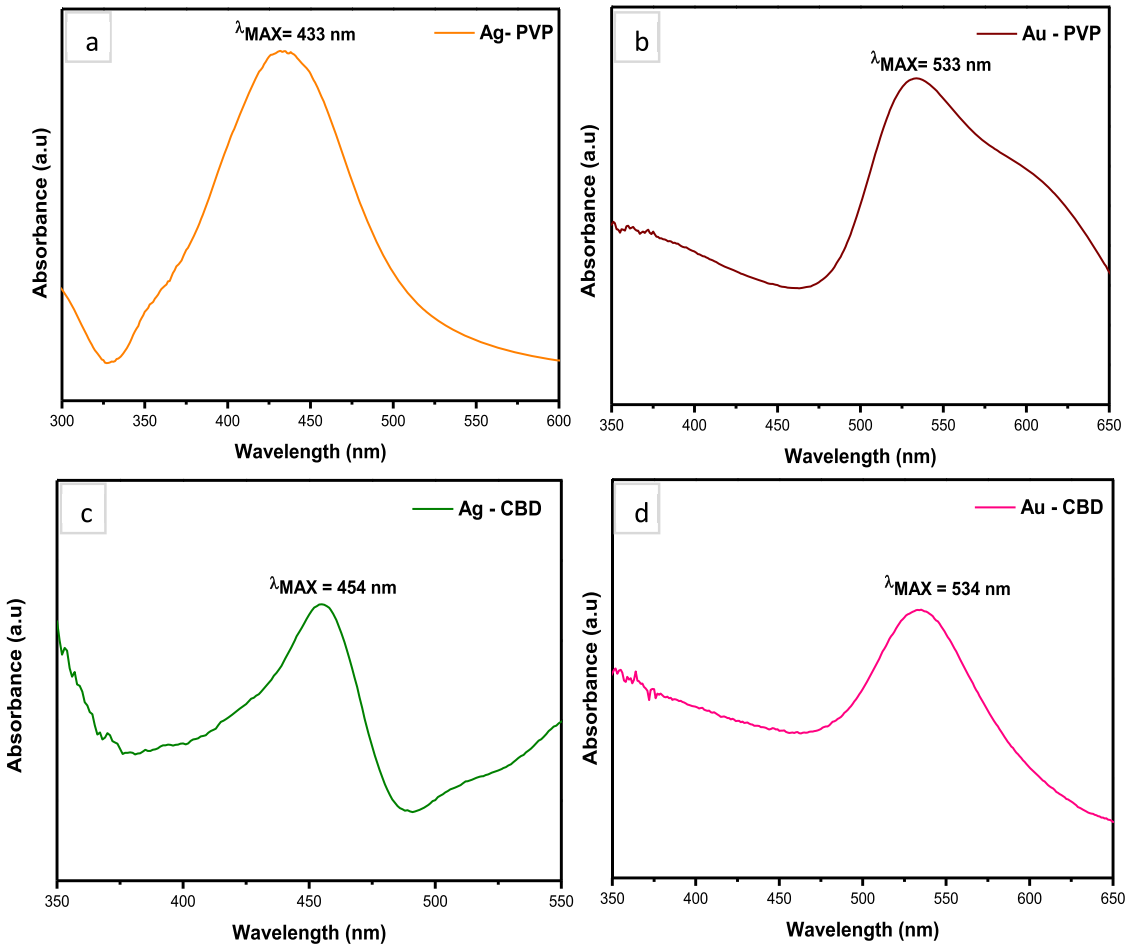

Figure 4. Optical analyses of NPs. (a) and (b) PVP-capped Ag and Au NPs and (c) and (d) CBD-capped Ag and Au NPs.

not in excess but just enough to prevent aggregation of NPs. Figure 3b,e presents histograms of AgNP size distribution, where Ag-CBD NPs have a smaller mean value of 4.82 nm ± 2.04 nm, when compared to Ag-PVP NP mean value of 6.43 nm ± 1.34 nm. Kumar et al.[55] explored PVP-capped AgNPs using a wet chemical reduction synthesis method and also reported a homogenous distribution of spherical NPs; however, the NP size range was between 15 and 25 nm, which is larger than the AgNPs obtained from the microwave synthesis in the current study.[55] A study by Liu et al.[56] synthesized AgNPs using phenolic acids derived from rice husks. The authors also observed well-dispersed spherical NPs; however, the average particle size (15 nm) was larger when compared to the TEM results in the current work. Liu et al.[56] attributed the well-dispersed AgNPs to phenolic acids that have a superior dispersion effect and prevented AgNP agglomeration.[56] The atomic structure of a single Ag crystal was explored by HR-TEM analysis. Figure 3c,f confirms the crystalline nature of synthesized AgNPs with lattice fringe spacings of 0.232 and 0.2504 nm, respectively, which correspond to the (111) planes of AgNPs.[57]

The synthesis of both PVP- and CBD-capped AuNPs yielded a color change from pale yellow to dark yellow, providing the first indication of $HAuCl_4$ reduction and subsequent AuNP formation. This correlates to previous reports on AuNP synthesis, where researchers have associated the formation of AuNPs with a color change from yellow to red.[58,59] This occurrence is based on the fact that noble metals exhibit a localized surface plasmon effect within the nanoscale range due to incident light, inducing surface electron oscillations in MNPs. Additionally, an increase in color intensity indicates the formation of large-sized NPs.[60] Figure 3g,h exhibits spherical monodispersed Au-PVP NPs and Au-CBD NPs, respectively; however, Au-PVP NPs are uniformly sized compared to Au-CBD NPs. Figure 3h,k presents histograms of AuNP distribution; Au-PVP NPs are smaller in size with a mean value of 5.52 nm ± 2.54 nm, whereas Au-CBD NPs have a mean value of 8.40 nm and the standard deviation is 5.50 nm. A research group that investigated PVP-capped AuNPs via a wet chemical method had also reported on spherical AuNPs; however, it observed a particle size of approximately 13 nm,[61] which is larger when compared to that of the AuNPs in the current study. Another research group synthesized AuNPs using an aqueous fruit extract from *Dillenia indica*, which is known to have high phenolic content and reported polydispersed NPs of various shapes, such as tetragonal, triangular, pentagonal, and spherical. Further analysis of the spherical AgNPs revealed a particle size range of 5−50 nm.[62] Figure 3I,l displays the lattice fringes of a single Au particle, where the d-spacings were measured to be 0.233 and 0.2314 nm, respectively, which correlates to the (111) index plane.[63]

2.2. Optical Properties. The optical properties of Ag and Au NPs were measured by UV−vis. One of the most characteristic physical properties of metallic AgNPs is the localized surface plasmon resonance (LSPR), which is responsible for the bright color and absorption characteristics of the NP colloidal suspensions.[64,65] Localized surface plasmon

https://doi.org/10.1021/acsomega.1c04303
ACS Omega 2021, 6, 29078−29090

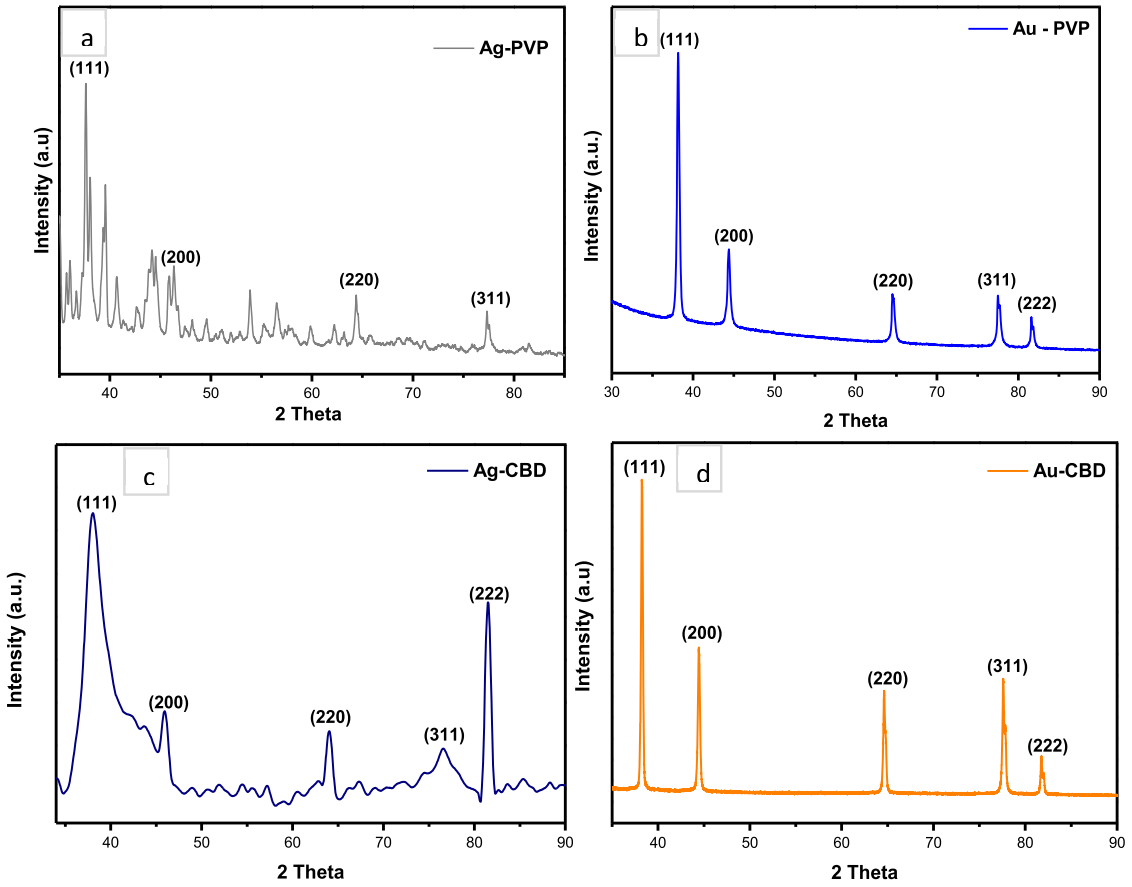

Figure 5. Structural analyses of NPs. (a) and (b) PVP-capped Ag and Au NPs and (c) and (d) CBD-capped Ag and Au NPs.

resonance occurs due to conductive NPs, which entrap light waves. Hence, LSPR is generated due to the incident light and conduction band surface electron interaction.[66] The UV−vis absorption range of AgNPs is between 400 and 500 nm due to silver's conduction band electrons and their excitation with respect to the LSPR phenomenon.[67] Figure 4a,c (Ag-PVP NPs and Ag-CBD NPs, respectively) exhibits bell-shaped SPR peaks, with absorption maxima of 433 nm and 454 nm, respectively. Rahman et al.[68] explained that the bell-shaped UV−vis peak represents spherical NPs. The absorption peak of 433 nm demonstrated by the Ag-PVP NPs indicates a slight red shift.[67] A study by Stevenson et al.[69] reported a narrow absorption peak also at 433 nm for spherical citrate-capped AgNPs, which were approximately 10 nm in size. The narrow LSPR peak indicates the formation of AgNPs with a narrow size distribution range.[69] The UV−vis analysis of Ag-CBD NPs in the current work correlates to the study by Liu et al.[56] previously discussed in Section 2.1, wherein UV absorption peaks of AgNPs between 445 and 455 nm were observed.[56]

Figure 4b,d presents the UV−vis spectra of AuNPs, where the absorption maxima for Au-PVP NPs are 533 nm and Au-CBD NPs are 534 nm. This provides further validation of AuNP formation, as previous reports indicate that the LSPR of AuNPs exhibit a strong absorbance band in the visible light region between 500 and 600 nm.[70] Additionally, a paper by Ogarev et al.[71] explains that as the size of spherical AuNPs increases, the LSPR peak position shifts increasingly to the right. This research group also reported that AuNPs within the size range of 5−100 nm exhibit an LSPR peak at 520 nm, which has been calculated based on the Mie theory.[72] However, the primary factor that influences the LSPR peak position in AuNPs is the dielectric constant of the environment, which is affected by several solvents and molecules that are adsorbed by nanospheres.[71] Both Au-PVP and Au-CBD NPs display a slight red shift in peak positions, which is caused by interactions between the solvent, molecules of PVP or CBD, and the Au NPs. In the case of Au-PVP NPs, this may be due to the clustering effect of AuNPs, which is observed in TEM (Figure 3g). Additionally, the Au-CBD NP UV−vis findings correlate to a study conducted by Sett et al.[62] This research group had observed SPR bands with absorption peaks ranging from 530 to 535 nm and further stated that it is a characteristic of spherical AuNPs.[62] The UV−vis findings further validate the formation of both Ag and Au NPs and concur with the results presented in Figure 3a−l.

2.3. Structural Analyses. Structural analyses of Ag and Au NPs were performed by XRD to determine the diffraction patterns of Ag and Au NPs and the crystalline or amorphous nature of the diffraction peaks. Both Ag-PVP (Figure 5a) and Ag-CBD (Figure 5c) NPs illustrate diffraction patterns with peaks at 2θ values of 38, 44, 64, and 77°, which correspond to (111), (200), (220), and (311) planes, respectively.[73] These diffractions represent the face-centered cubic (fcc) structure of metallic silver (JCPDS File No. 04-0783). Additionally, the intense peaks at 2θ = 38° in both Ag-PVP and Ag-CBD NP diffraction patterns indicate that the AgNPs have a preferred orientation along the (111) plane.[73] This correlates with the data analysis derived from HR-TEM, Figure 3c,f. The unidentified peaks in Figure 5a could potentially be attributed to the presence of silver oxide present in the sample.[73] A previous study on PVP-capped AgNPs also reported on

https://doi.org/10.1021/acsomega.1c04303
ACS Omega 2021, 6, 29078−29090

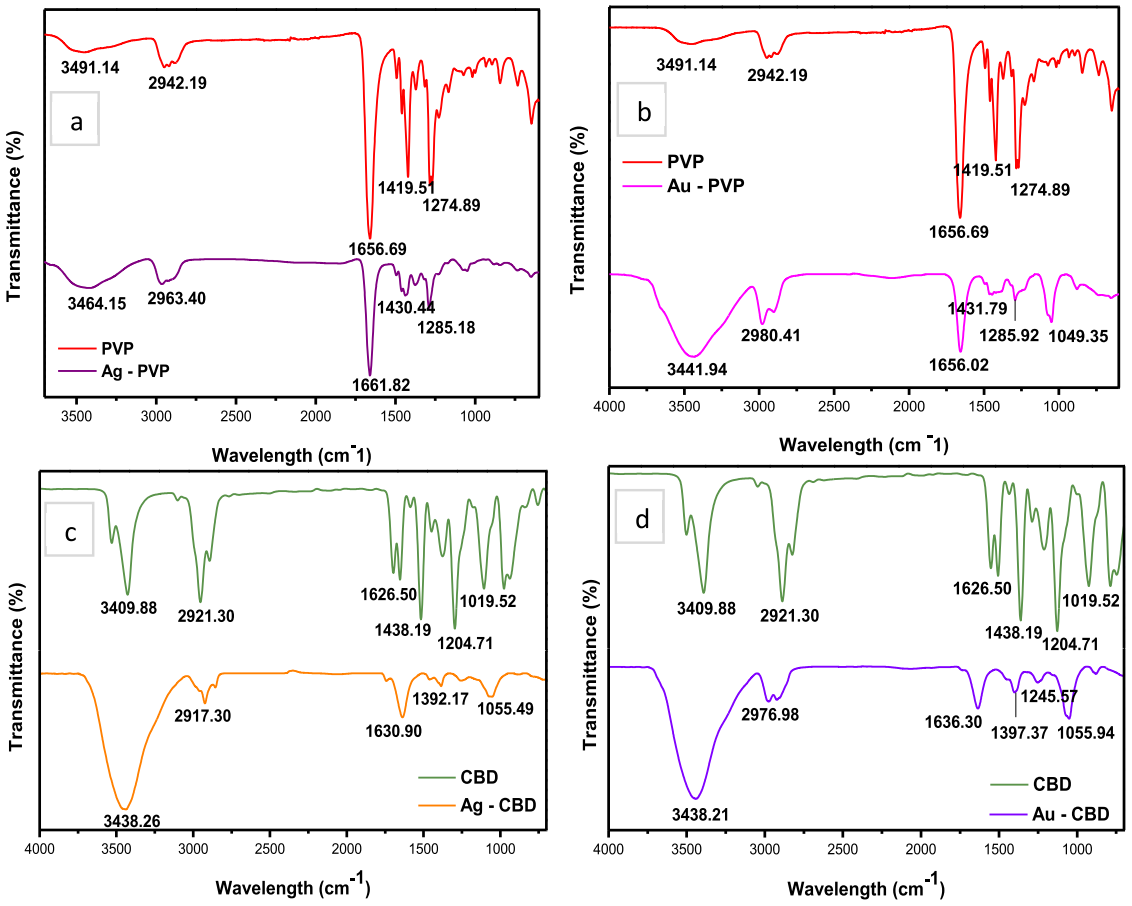

Figure 6. FT-IR spectra of NPs. (a) and (b) PVP-capped Ag and Au NPs and (c) and (d) CBD-capped Ag and Au NPs.

diffraction peaks that correspond to the (111), (200), (220), and (311) planes.[55] This is in agreement with the XRD analysis in the current study as it provides validation for the findings. The broad diffraction peaks in Figure 5c indicate a small crystallite size.[74]

Figure 5b,d displays the diffraction patterns of Au-PVP and Au-CBD NPs, respectively. Both diffraction patterns exhibit peaks at 2θ = 38, 44, 64, 77, and 82°, which correspond to the standard Bragg reflections of (111), (200), (220), (311), and (222), respectively. These diffractions represent the fcc structure of metallic gold (JCPDS File No. 01-1174).[75] All five peaks in both Au-PVP and Au-CBD NP diffraction patterns are sharp and narrow, which suggests pure, well-crystallized AuNPs.[76] Similar to the synthesized AgNPs in this study, there is intense diffraction at 2θ = 38°, as shown in Figure 5b,d, which demonstrates that the preferred growth orientation is along the (111) plane.[75] A study by State et al.[77] explored the synthesis and characterization of PVP-capped AuNPs and reported similar XRD findings to the current work. The diffraction pattern presented by State et al.[77] had exhibited four peaks that correspond to the (111), (200), (220), and (311) planes; however, the peaks were observed to be broad when compared to the Au-PVP XRD pattern in the current study. Broad diffraction peaks are generally linked to a smaller NP size.[77]

2.4. Chemical Analyses. Figure 6a,b shows the FT-IR spectra of PVP in comparison to Ag-PVP and Au-PVP NPs, respectively, within a frequency range of 4000−500 cm^{-1}. The FT-IR spectra of Ag-PVP and Au-PVP NPs exhibit all of the signature resonance peaks of PVP, which indicates that both Ag and Au NPs have been successfully capped by PVP. However, the peaks observed at 1414 and 1276 cm^{-1} in the PVP spectrum corresponding to CH_2 bending and C−N stretching vibrations[50] have shifted to 1430 and 1285 cm^{-1}, respectively, in the spectrum of Ag-PVP NPs. Furthermore, the intensity of these two IR peaks decreased. The peak shift and decrease in intensity indicate the chemical interaction of PVP with the surface of AgNPs.[55] Sahoo et al.[78] investigated the role of PVP as a stabilizing agent in AgNP synthesis and also observed a peak shift and a decrease in intensity within the C−N vibrational group. Sahoo and co-authors explained that the shift seen in the C−N bond was indicative of nitrogen atom coordination to AgNPs. This phenomenon is a result of nitrogen's lone pair electrons being donated.

Moreover, when the nitrogen atom has coordinated to AgNPs, NP stability is generated, which restricts additional particle growth and agglomeration.[78] An intense broad IR peak is seen in Au-PVP NPS at 3441 cm^{-1} corresponding to the O−H stretching vibration of alcohols, which is due to the incorporation of ethanol in the synthesis method. A minimal peak position shift and a considerable peak intensity reduction were also observed at 1419 and 1274 cm^{-1} to 1431 and 1285 cm^{-1}, respectively. These peaks correspond to CH_2 bending and C−N stretching vibrations. This indicates a surface functionalization due to a chemical interaction between PVP and AuNP. The IR peak at 1049 cm^{-1} corresponds to a C−N stretching vibration.[79] Mohamed et al.[79] investigated PVP-capped AuNPs and reported four characteristic peaks of PVP, which correspond to the O−H, CH_2, C═O, and C−N vibrational groups. These

https://doi.org/10.1021/acsomega.1c04303
ACS Omega 2021, 6, 29078−29090

findings correlate to the Au-PVP FT-IR analysis in the current study.

Figure 6c,d presents the comparative FT-IR spectra of CBD, Ag-CBD, and Au-CBD NPs. Overall, the IR spectra of both Ag-CBD and Au-CBD NPs exhibit characteristic resonance peaks of CBD, indicating successful capping of Ag and Au NPs by CBD. The IR peaks at positions 3409, 2921, 1626, and 1438 cm^{-1} in the CBD spectrum have shifted to peak positions of 3438, 2917, 1630, and 1392 cm^{-1} in the Ag-CBD spectrum (Figure 6c), which correlate to the O−H stretching, C−H stretching, C═C stretching, and C−H bending vibrational groups, respectively.[80] A shift in the peak position either to a higher or a lower wavelength number indicates that the electron distribution within the molecular bond or the hybridization state has been altered. This could potentially be due to the chemical interaction between chemical/natural compounds that function as capping and reducing agents and the bulk material, in this case, a metallic precursor salt,[81] and could also explain the larger red shift observed in the UV−vis peak of Ag-CBD NPs in comparison to that of Ag-PVP NPs. The FT-IR analysis of Ag-CBD NPs can be closely correlated to a study by Firoozi et al.[82] where AgNPs were synthesized using an aqueous extract from *Satureja intermedia* C.A. Mey. The IR spectrum of plant extract-capped AgNPs also exhibited peaks of the O−H, C−H, and C═C functional groups.

Furthermore, the authors attributed the reduction of silver ions and stabilization of AgNPs to the flavonoids and phenolic compounds that are present in the plant extract.[82] Figure 6d (Au-PVP NPs) reveals the intense peak at 3438 cm^{-1} that correlates to the O−H stretching vibration. This indicates an increased amount (per unit volume) of O−H groups that are available for molecular bond reactions.[81] The IR peaks at 2976, 1636, 1397, and 1245 cm^{-1} all exhibit a minimal peak position shift with a decrease in the peak intensity. Furthermore, these IR peaks represent the following functional groups in CBD: C−H stretching, C═C, C−H bending, and C−O.[80] Additionally, Das et al.[83] synthesized AuNPs using an ethanolic leaf extract from *Centella asiatica* and reported similar IR spectra peaks when compared to the Au-CBD NPs in the current work. The research group also indicated a possible chemical interaction between the phenolic compounds and the surface of AuNPs, which had resulted in AuNP stabilization.[83]

The differences in the NP size and morphology observed between the previous literature and the current work can be attributed to varying factors such as capping and reducing agents, synthesis methods, reaction parameters, and precursor salts.

2.5. Cytotoxicity Analysis. The present study explored the potential cytotoxic effect of CBD and PVP/CBD-capped NPs in HaCat cell lines. The HaCaT cell lines were exposed to varying concentrations of CBD (2.2−200 μM) and PVP/CBD-capped NPs (3−600 μg/mL) over 48 h to generate dose−response curves and accompanying IC_{50} values (Table 4; Figure 7). There have been no scientific reports to the author's knowledge that have investigated CBD-capped NPs for cytotoxicity against HaCaT cells. To compensate for the paucity of the literature, studies that involve phenolic compounds or terpenes as a capping and reducing agent in NP synthesis were used for comparison.

All samples displayed cytotoxicity toward HaCaT cells; however, CBD exhibited the highest cytotoxicity, with an IC_{50} value of 5.82 μM (equivalent to 1.83 μg/mL). Results align to that of Ligresti et al.,[84] where CBD induced a reduction in the cell number of 70% at 25 μM in HaCaT cells. To assess the potential synergistic effect between CBD and metal (Au and Ag) NPs, the IC_{50} values of PVP-capped NPs were compared to CBD-capped NPs. Table 4 indicates that CBD-capped AgNPs did not increase cytotoxicity; therefore, this study did not demonstrate synergism between CBD and Ag NPs. However, a combinational effect was observed between CBD and Au NPs, as the IC_{50} of Au-CBD (23.99 μg/mL) is lower than Au-PVP (67.86 μg/mL), indicating an increased cytotoxicity profile for Au-CBD NPs. Cannabidiol-capped NPs showed much lower cytotoxicity compared to CBD with Ag-CBD (8.84% cell density reduction at 100 μg/mL, thus IC_{50} not available) and Au-CBD (IC_{50} 23.99 μg/mL). The Au-CBD NP cytotoxicity plateaued at concentrations >50 μg/mL, suggesting either a maximal cytotoxic property, an antiproliferative effect, or a reduction in the biological effect due to NP characteristic changes at higher concentrations. These findings correlate to a previous study that reported on the inhibitory and antiproliferative effects of CBD on differentiated HaCaT cells and transformed human keratinocytes, respectively.[85]

Table 4. IC_{50} Values of Cannabidiol- and Polyvinylpyrrolidone/cannabidiol-Capped Nanoparticles in Human Keratinocyte Cells

drug compound	IC_{50}[b] ± SEM[c] on HaCaT[d]
CBD[a]	5.82 ± 1.06 μM
CBD-Ag[e] NPs[f]	>100 μg/mL
CBD-Au[g] NPs	23.99 ± 1.10 μg/mL
PVP[h]-Ag NPs	>100 μg/mL
PVP-Au NPs	67.86 ± 1.10 μg/mL

[a]Cannabidiol. [b]Half-maximal inhibitory concentration. [c]Standard error of the mean. [d]Cultured human keratinocyte cells. [e]Silver. [f]Nanoparticles. [g]Gold. [h]Polyvinylpyrrolidone.

Given the experimental washing procedures, retention of NPs within the analysis well was excluded. Phenolic-containing plant extracts used in NP synthesis have been used as comparators. The IC_{50} values of Ag and Au NPs in the current study vary when compared to the previous literature. Lakshmipathy and Nanda[87] investigated the cytotoxicity of gallic acid-capped AgNPs in monkey kidney (Vero) cell line and reported an 8% cell viability when tested at 100 mg/mL. Nirmala et al.[88] used *Vitis vinifera* seeds, which are rich in polyphenols to synthesize AuNPs and reported no cytotoxicity when tested in HaCaT cells, with the concentration range of 5−25 μM. A primary factor can be attributed to differences in the phenolic compound chemical structure, which will impact their biological properties. Phenolic compounds are categorized into five subtypes, namely, phenolic acids, flavonoids, tannins, coumarins, and stilbenes.[86] Other contributing factors are varying cell lines, exposure time, NP size, cytotoxicity assay, and NP concentration.

Previous literature reveals that multiple factors are linked to therapeutic delivery systems and play a role in enhanced biological activity. These factors are briefly discussed below.

Altering the physical properties of a NP, such as size, shape, and surface charge, influences their biological activity[89] and could result in enhanced therapeutic effects.[90] The morphology of a particle is also an essential factor in NP uptake and biodistribution.[91] The initial interaction between NPs and target cells occurs at a specific contact angle orientation, which determines its rate of uptake.[91] NPs that are incorporated at a slower rate are oriented with its' long axis parallel to the cell membrane, whereas a NP that is oriented with its' short axis

https://doi.org/10.1021/acsomega.1c04303
ACS Omega 2021, 6, 29078−29090

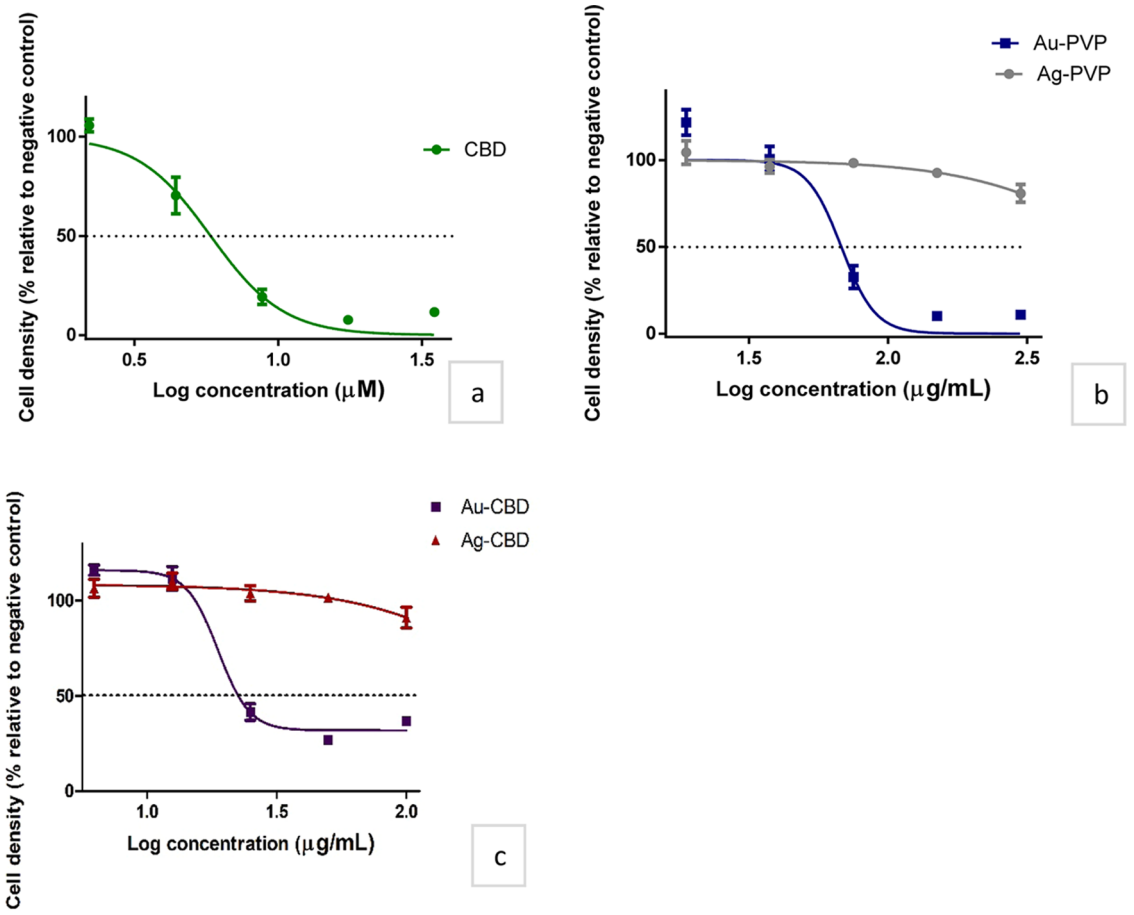

Figure 7. Effect of (a) cannabidiol, (b) polyvinylpyrrolidone-capped nanoparticles, and (c) cannabidiol-capped nanoparticles in human keratinocyte cell density. The black dashed line represents a 50% cell density.

parallel to the cell membrane is more quickly incorporated into the target tissue. The symmetrical shape of spherical NPs renders the rate of incorporation to be independent of theta (θ).[91] Therefore, the shape and contact angle of a NP play a role in the efficiency of NP internalization. Constituents of a biological medium may influence NPs as well, where protein absorption may take place with the subsequent formation of protein-coated NPs. Protein coating alters the surface charge, dispersion, size, biodistribution, and biological effect of a NP, which may be beneficial or detrimental to its purpose.[92] In this study, NPs were dispersed in FBS, prior to cells being exposed, which may alter their biological properties. Characterization of NPs in FBS-supplemented medium was not done; however, it may shed light on the structural and functional changes that may have occurred upon protein binding.

3. CONCLUSIONS

This study demonstrated a time and energy-efficient one-pot green synthesis approach that resulted in the formation of stable Ag and Au NPs. These MNPs were rapidly biosynthesized using the microwave-assisted synthesis route and CBD as both the capping and reducing agent. The characterization analysis of CBD-capped NPs revealed that CBD was successful in synthesizing both Ag and Au NPs. This could be due to the phenolic groups present in CBD, as the previous literature indicates that phenolic compounds are well known for their reducing and stabilizing properties in NP synthesis. Cannabidiol-capped MNPs (Ag and Au) were observed to be spherical, monodispersed, and smaller than 10 nm. The cytotoxicity analysis revealed that CBD-capped NPs exhibited a much lower cytotoxic effect on HaCaT cells when compared to CBD alone. Furthermore, capping Au NPs with CBD resulted in an increased cytotoxic effect, which could potentially be beneficial in cancer treatment. Given the evidence of CBD's potential therapeutic properties, further assessment into their potential use as drug delivery systems for skin-related disorders is rational. The CBD-capped Ag and Au NPs synthesized in this study should be considered in targeted transdermal drug delivery systems due to the small NP size and low cytotoxic profile within an *in vitro* setting in HaCaT cells.

4. EXPERIMENTAL SECTION

4.1. Materials for Nanoparticle Synthesis. All chemical reagents including silver nitrate ($AgNO_3$) (Minema Chemicals, South Africa), polyvinylpyrrolidone (PVP) (Sigma-Aldrich, South Africa), gold (III) chloride trihydrate ($HAuCl_4{\cdot}3H_2O$) (Sisco Research Laboratories, India), ethanol (99%) (Ethanol-SA, South Africa), and CBD crystals (99%) (Endoca BV, Netherlands) were kindly supplied by BGM Pharmaceuticals, South Africa and were used as received. Deionised (DI) water was used in several synthesis process steps. To obtain optimized NPs, several parameters had to be varied (Table 5).

4.2. Microwave-Assisted Chemical and Green Synthesis of NPs. One of the objectives of this study was to chemically synthesize Ag and Au NPs using PVP, which functioned as reference materials in assessing CBD as an

https://doi.org/10.1021/acsomega.1c04303
ACS Omega 2021, 6, 29078−29090

Table 5. Optimization Parameters for Synthesis of Nanoparticles

capping agent PVP[a] (g)	concentration of CBD[b] (M)	volume of capping reagent solution (mL)	volume of 0.1 M precursor salt (mL)	synthesis time (min)	synthesis temperature (°C)
0.5	0.00025	40	1, 2 or 5	30	100
0.25	0.001	25	10	20	70
0.1	0.01	10	25	10	50

[a]Polyvinylpyrrolidone. [b]Cannabidiol.

effective capping and reducing agent in NP synthesis. The synthesis of NPs was based on a protocol by Pal et al.,[93] with minor adjustments implemented. Briefly, $AgNO_3$ and $HAuCl_4 \cdot 3H_2O$ were used as precursor salts for Ag and Au NPs, respectively. A 0.1 M solution was made by dissolving a known amount of precursor salt in DI water. Varying volumes of the 0.1 M solution were added to a known PVP or CBD concentration prepared in ethanol (Table 5). This homogenous mixture was then transferred into Teflon-coated vessels and loaded into a Milestone Ultraclave (MA 033). Multiple synthesis reactions were run by varying synthesis time and temperature. After each run, the resultant solution was washed with DI water and centrifuged at 1917 relative centrifugal force (RCF) for 20 min using a Rotofix 32A centrifuge (Hettich). The washing and centrifugation steps were repeated three times, and the precipitate was finally washed with ethanol to ensure the removal of all unreacted materials. The samples were then freeze-dried at −40°C over six days using an AdVantage Pro freeze dryer/lyophilizer (SP Scientific) and subsequently stored in a closed container at room temperature for further characterization.

4.3. Characterization of NPs. *4.3.1. Transmission Electron Microscopy.* The particle sizes of Ag and Au NPs were determined by a JEOL TEM-2100 (JEOL, Japan) using transmission electron microscopy (TEM) at an accelerating voltage of 200 kV. A minute amount of the freeze-dried sample was dispersed in approximately 1 mL of ethanol, which was sonicated for 20 min. A copper grid was dipped into the mixture and allowed to air dry. Thereafter, the copper grid was mounted onto the sample holder and inserted into the microscope. Images were captured at different magnifications and saved for further analysis. The particle size distribution was investigated by ImageJ software by analyzing 300−400 particles per sample. The NPs were analyzed by high-resolution TEM (HR-TEM) to attain information about the position of lattice fringes that are associated with the atomic planes that exist within the NP.

4.3.2. Ultraviolet−Visible Spectroscopy. Ultraviolet−visible (UV−vis) spectroscopy was used to study the optical properties of synthesized NPs. A Lambda 750s (PerkinElmer) was used for analysis, where the absorbance of light by each sample was measured over a wavelength range of 200−800 nm with a spectral resolution of 1 nm. Samples were dispersed in ethanol before analysis.

4.3.3. X-ray Diffraction. The crystalline structure of synthesized NPs was analyzed by the powder X-ray diffraction (PXRD) technique employing a PANalytical XPERT-PRO diffractometer (PANalytical, the Netherlands) using nickel-filtered copper Kα radiation (λ= 1.5406 Å), with the tension voltage and current set at 45 kV and 40 mA, respectively. The diffraction measurements were performed at room temperature in a Bragg−Brentano geometry with a scan range of 2θ = 5−90° using a scan rate of 0.02°/s.

4.3.4. Fourier Transform Infrared Spectroscopy. Fourier transform infrared (FT-IR) spectroscopy analysis was performed to confirm the capping efficiency of PVP and CBD for the synthesized NPs. A Spectrum 100 FT-IR spectrometer (PerkinElmer) was employed for sample analysis. The attenuated total reflectance Fourier transform infrared (ATR-FT-IR) spectra for the samples were obtained over a wavenumber range of 4000−500 cm^{-1}, the spectral resolution was set at 4 cm^{-1}, and the number of scans per spectrum was 32.

4.3.5. Materials for Cytotoxicity Evaluation. The following materials were used in the cytotoxicity evaluation of CBD and CBD-capped NPs in HaCaT cells: HaCaT cell line (human epidermal keratinocytes; American Type Culture Collection); CBD (Endoca BV Netherlands); Dulbecco's modified Eagle's medium (DMEM), fetal bovine serum (FBS), phosphate-buffered saline (PBS) (Gibco—Thermo Fisher Scientific, South Africa); and acetic acid, dimethyl sulfoxide (DMSO), ethylenediaminetetraacetic acid (EDTA), fungizone, penicillin, sodium hydroxide (NaOH), streptomycin, sulforhodamine B salt, trichloroacetic acid (TCA), trisaminomethane (Tris), trypan blue, and trypsin (Sigma-Aldrich, South Africa).

4.3.6. Cell Culture. The HaCaT cell lines were maintained in 75 cm^2 culture flasks containing complete medium (DMEM with 10% heat-inactivated FBS and 1% antibiotics [100 U/mL penicillin, 100 μg/mL streptomycin, and 250 μg/mL fungizone]) at 37 °C in a humidified incubator set at 5% CO_2. Cells were subcultured once a confluence of 70−80% was reached. Cultures were rinsed with PBS and chemically detached using trypsin−EDTA (0.25% trypsin containing 0.01% EDTA) for 10 min. Cells were harvested and trypsin-deactivated using a complete medium. Cells were centrifuged at 200 RCF for 5 min using a Sigma 3K15 centrifuge (Sigma, Germany). The supernatant was discarded, and the pellet of cells is resuspended in 1 mL of 10% FBS-supplemented medium. A 1:9 dilution of cells was made with 0.1% trypan blue, and the cells were counted using a hemocytometer. The cell concentration was adjusted to 100 000 cells/mL.

4.3.7. Sulforhodamine B Staining. The HaCaT cells (100 μL) were seeded in a 96-well microtitre plate. The plate was incubated for 24 h at 37 °C and 5% CO_2 to allow the cells to attach to the plate surface. The NPs were each prepared to a stock solution of 0.6 mg/mL and were filtered using a sterile syringe filter (0.2 μm). Aliquots of CBD were prepared in DMSO to 25 mM. Cells were exposed to 100 μL of medium (negative control), DMSO (0.8%; vehicle control), CBD (2.2−200 μM), or NPs (3−600 μg/mL) prepared in FBS-free medium for 48 h. A row of blanks (5% FBS-supplemented medium) was also allocated on each plate to account for sterility and background noise. After exposure, 50 μL of 50% TCA was added to each well and incubated at 4 °C for a further 24 h to fix the cells. Thereafter, TCA was washed off with tap water and allowed to air-dry. A volume of 100 μL of SRB dye (0.057% in 1% acetic acid) was added to each well, and the plate was incubated for 1 h. The unbound SRB dye was washed off with 100 μL of 1% acetic acid thrice, and the plates were allowed to dry. Tris-buffer solution (200 μL; 10 mM, pH 10.5) was added to all wells to solubilize the bound dye. Plates were measured spectrophotometrically using an ELX 800 plate reader (BioTek Industries) at 540 nm (reference wavelength = 630 nm). Values were blank-excluded, and the cell density was calculated using the following formula

https://doi.org/10.1021/acsomega.1c04303
ACS Omega 2021, 6, 29078−29090

$$\text{cell density (\% of negative control)} = \left(\frac{\text{absorbance of sample}}{\text{average absorbance of negative control}} \right) \times 100$$

The assay was performed with technical and biological triplicates. GraphPad Prism software was employed for statistical analysis of the half-maximal inhibitory concentration (IC_{50}).

AUTHOR INFORMATION

Corresponding Author

Suprakas Sinha Ray − *Centre for Nanostructured and Advanced Materials, DSI-CSIR Nanotechnology Innovation Centre, Council for Scientific and Industrial Research, Pretoria 0001, South Africa; Department of Chemical Sciences, University of Johannesburg, 2028 Johannesburg, South Africa;* orcid.org/0000-0002-0007-2595; Email: rsuprakas@csir.co.za, ssinharay@uj.ac.za

Authors

Andrea Jess Josiah − *Centre for Nanostructured and Advanced Materials, DSI-CSIR Nanotechnology Innovation Centre, Council for Scientific and Industrial Research, Pretoria 0001, South Africa; Department of Chemical Sciences, University of Johannesburg, 2028 Johannesburg, South Africa*

Sreejarani K. Pillai − *Centre for Nanostructured and Advanced Materials, DSI-CSIR Nanotechnology Innovation Centre, Council for Scientific and Industrial Research, Pretoria 0001, South Africa*

Werner Cordier − *Department of Pharmacology, Faculty of Health Sciences, University of Pretoria, Pretoria 0002, South Africa*

Margo Nell − *Department of Pharmacology, Faculty of Health Sciences, University of Pretoria, Pretoria 0002, South Africa*

Danielle Twilley − *Department of Plant and Soil Sciences, Faculty of Natural and Agricultural Sciences, University of Pretoria, Pretoria 0002, South Africa*

Namrita Lall − *Department of Plant and Soil Sciences, Faculty of Natural and Agricultural Sciences, University of Pretoria, Pretoria 0002, South Africa; School of Natural Resources, University of Missouri, Columbia, Missouri 65211, United States; College of Pharmacy, JSS Academy of Higher Education and Research, Mysuru 570015, India;* orcid.org/0000-0002-3242-3476

Complete contact information is available at: https://pubs.acs.org/10.1021/acsomega.1c04303

Author Contributions

Experimental work, conceptualization, and preparation of original draft: A.J.J., S.K.P., and W.C.; expert opinion and critical review: S.S.R. and N.L.; and technical expertise for cytotoxicity analysis: M.N. and D.T.

Notes

The authors declare no competing financial interest.

ACKNOWLEDGMENTS

The authors (S.S.R., A.J.J., S.K.P.) thank the Department of Science and Innovation (C6ACH77) and the Council for Scientific and Industrial Research (086ADMI) for financial support. The authors thank BGM Pharmaceuticals and Martin Magwaza for providing the reagents required to conduct this study.

REFERENCES

(1) Hulla, J. E.; Sahu, S. C.; Hayes, A. W. Nanotechnology: History and future. *Hum. Exp. Toxicol.* **2015**, *34*, 1318−1321.

(2) Emerich, D. F.; Thanos, C. G. Nanotechnology and medicine. *Expert Opin. Biol. Ther.* **2003**, *3*, 655−663.

(3) Buzea, C.; Pacheco, I. I.; Robbie, K. Nanomaterials and nanoparticles: Sources and toxicity. *Biointerphases* **2007**, *2*, MR17−MR71.

(4) Roduner, E. Size matters: Why nanomaterials are different. *Chem. Soc. Rev.* **2006**, *35*, 583−592.

(5) He, Z.; Zhang, Z.; Bi, S. Nanoparticles for organic electronics applications. *Mater. Res. Express* **2020**, *7*, No. 012004.

(6) Blanc, W.; Vermillac, M.; Peters, F.; Kucera, C.; Tuggle, M. A.; Hawkins, T. W.; Ballato, J. *Drawing Optical Fibers: Elongating Bubbles, Breaking Nanoparticles. 1st International Conference on Optics, Photonics and Lasers (OPAL' 2018).*

(7) Ganaie, S. U.; Abbasi, T.; Anuradha, J.; Abbasi, S. A. Biomimetic synthesis of silver nanoparticles using the amphibious weed ipomoea and their application in pollution control. *J. King Saud Univ. Sci.* **2014**, *26*, 222−229.

(8) Patel, A.; Prajapati, P.; Boghra, R. Overview on Applications of Nanoparticles in Cosmetics. *AJPSCR* **2011**, *1*, 40−55.

(9) Nune, S. K.; Gunda, P.; Thallapally, P. K.; Lin, Y. Y.; Forrest, M. L.; Berkland, C. J. Nanoparticles for Biomedical Imaging. *Expert Opin. Drug Deliv.* **2009**, *6*, 1175−1194.

(10) Alberti, T. B.; Coelho, D. S.; de Prá, M.; Maraschin, M.; Veleirinho, B. Electrospun PVA nanoscaffolds associated with propolis nanoparticles with wound healing activity. *J. Mater. Sci.* **2020**, *55*, 9712−9727.

(11) Lombardo, D.; Kiselev, M. A.; Caccamo, M. T. Smart Nanoparticles for Drug Delivery Application: Development of Versatile Nanocarrier Platforms in Biotechnology and Nanomedicine. *J. Nanomater.* **2019**, *2019*, 1−26.

(12) Campos, P. M.; Bentley, M. V. L. B.; Torchilin, V. P. Nanopreparations for Skin Cancer Therapy. In *Nanobiomaterials in Cancer Therapy: Applications of Nanobiomaterials*, 1st ed.; Elsevier Inc, 2016; Vol. 7, pp 1−28.

(13) Simões, M. C. F.; Sousa, J. J. S.; Pais, A. A. C. C. Mini-review Skin cancer and new treatment perspectives: A review State of the art for skin cancer Skin cancer. *Cancer Lett.* **2015**, *357*, 8−42.

(14) File:3D medical animation skin layers.jpg - Wikimedia Commons. https://www.scientificanimations.com/, CC BY-SA 4.0 <https://creativecommons.org/licenses/by-sa/4.0>, via Wikimedia Commons https://commons.wikimedia.org/wiki/File:3D_medical_animation_skin_layers.jpg.

(15) Marks, J.; Miller, J. Structure and Function of Skin. In *Lookingbill and Marks' Principles of Dermatology*, 6th ed.; Elsevier Health Sciences, 2011; pp 1−2.

(16) Focus on Cosmeceuticals: Skin anatomy and photoageing | The PMFA Journal. https://www.thepmfajournal.com/features/post/focus-on-cosmeceuticals-skin-anatomy-and-photoageing, (accessed 2020-12-04).

(17) Anderson, K. *Mosby's Medical, Nursing, and Allied Health Dictionary*, 4th ed.; Mosby: St. Louis, 1994.

(18) Zeb, A.; Arif, S. T.; Malik, M.; Shah, F. A.; Din, F. U.; Qureshi, O. S.; Lee, E.; Lee, G.; Kim, J. Potential of Nanoparticulate Carriers for Improved Drug Delivery via Skin. *J. Pharm. Investig.* **2019**, *49*, 485−517.

(19) Desmet, E.; Van Gele, M.; Lambert, J. Topically applied lipid- and surfactant-based nanoparticles in the treatment of skin disorders. *Expert Opin. Drug Deliv.* **2017**, *14*, 109−122.

(20) Gupta, S.; Bansal, R.; Gupta, S.; Jindal, N.; Jindal, A. Nanocarriers and Nanoparticles for Skin Care and Dermatological Treatments. *Indian Dermatol. Online J.* **2013**, *4*, No. 267.

(21) Alkilani, A. Z.; McCrudden, M. T. C.; Donnelly, R. F. Transdermal drug delivery: Innovative pharmaceutical developments based on disruption of the barrier properties of the stratum corneum. *Pharmaceutics* **2015**, *7*, 438−470.

(22) Tanwar, H.; Sachdeva, R. Transdermal drug delivery system: A review. *Int. J. Pharm. Sci. Res.* **2016**, *7*, 2274−2290.

(23) Palmer, B. C.; Delouise, L. A. Nanoparticle-enabled transdermal drug delivery systems for enhanced dose control and tissue targeting. *Molecules* **2016**, *21*, No. 1719.
(24) Niska, K.; Zielinska, E.; Radomski, M. W.; Inkielewicz-Stepniak, I. Metal nanoparticles in dermatology and cosmetology: Interactions with human skin cells. *Chem.Biol. Interact.* **2018**, *295*, 38−51.
(25) Salber, J.; Gräter, S.; Harwardt, M.; Hofmann, M.; Klee, D.; Dujic, J.; Jinghuan, H.; Ding, J.; Kippenberger, S.; Bernd, A.; Groll, J.; Spatz, J.; Möller, M. Influence of different ECM mimetic peptide sequences embedded in a nonfouling environment on the specific adhesion of human-skin keratinocytes and fibroblasts on deformable substrates. *Small* **2007**, *3*, 1023−1031.
(26) Gupta, R.; Rai, B. Effect of size and surface charge of gold nanoparticles on their skin permeability: A molecular dynamics study. *Sci. Rep.* **2017**, *7*, No. 45292.
(27) Tian, J.; Wong, K. K.; Ho, C. M.; Lok, C. N.; Yu, W. Y.; Che, C. M.; Chiu, J. F.; Tam, P. K. Topical delivery of silver nanoparticles promotes wound healing. *ChemMedChem* **2007**, *2*, 129−136.
(28) Arora, S.; Tyagi, N.; Bhardwaj, A.; Rusu, L.; Palanki, R.; Vig, K.; Singh, S. R.; Singh, A. P.; Palanki, S.; Miller, M. E.; Carter, J. E.; Singh, S. Silver nanoparticles protect human keratinocytes against UVB radiation-induced DNA damage and apoptosis: Potential for prevention of skin carcinogenesis. *Nanomedicine Nanotechnology, Biol. Med.* **2015**, *11*, 1265−1275.
(29) Iravani, S.; Korbekandi, H.; Mirmohammadi, S. V.; Zolfaghari, B. Synthesis of silver nanoparticles: Chemical, physical and biological methods. *Res. Pharm. Sci.* **2014**, *9*, 385−406.
(30) Yadi, M.; Mostafavi, E.; Saleh, B.; Davaran, S.; Aliyeva, I.; Khalilov, R.; Nikzamir, M.; Nikzamir, N.; Akbarzadeh, A.; Panahi, Y.; Milani, M. Current developments in green synthesis of metallic nanoparticles using plant extracts: A Review. *Artif. Cells, Nanomedicine, Biotechnol.* **2018**, *46*, S336−343.
(31) Mohanpuria, P.; Rana, N. K.; Yadav, S. K. Biosynthesis of nanoparticles: Technological concepts and future applications. *J. Nanoparticle Res.* **2008**, *10*, 507−517.
(32) Jeevanandam, J.; Chan, Y. S.; Danquah, M. K. Biosynthesis of metal and metal oxide nanoparticles. *ChemBioEng Rev.* **2016**, *3*, 55−67.
(33) Shafey, A. M. El. Green synthesis of metal and metal oxide nanoparticles from plant leaf extracts and their applications: A review. *Green Process. Synth.* **2020**, *9*, 304−339.
(34) Devatha, C. P.; Thalla, A. K. Green Synthesis of Nanomaterials. In *Synthesis of Inorganic Nanomaterials*, 1st ed.; Elsevier, 2018; pp 169−184.
(35) Ramelet, A. A. Venoactive Drugs. In *Sclerotherapy: Treatment of Varicose and Telangiectatic Leg Veins*; Elsevier Inc: 2007; pp 373−381.
(36) File:Cannabidiol.png - Wikimedia Commons. https://commons.wikimedia.org/wiki/File:Cannabidiol.png.
(37) Abrams, D.; Guzman, M. Cannabis in cancer care. *Clin. Pharmacol. Ther.* **2015**, *97*, 575−586.
(38) Pisanti, S.; Malfitano, A. M.; Ciaglia, E.; Lamberti, A.; Ranieri, R.; Cuomo, G.; Abate, M.; Faggiana, G.; Proto, M. C.; Fiore, D.; Laezza, C.; Bifulco, M. Cannabidiol: State of the art and new challenges for therapeutic applications. *Pharmacol. Ther.* **2017**, *175*, 133−150.
(39) Pulvirenti, N.; Nasca, M. R. M. G. Topical adelmidrol 2% emulsion, a novel aliamide, in the treatment of mild atopic dermatitis in pediatric subjects: A pilot study. *Acta Dermatovenerol Croat.* **2007**, *15*, 80−83.
(40) Chelliah, M. P.; Zinn, Z.; Khuu, P.; Teng, J. M. C. Self-initiated use of topical cannabidiol oil for epidermolysis bullosa. *Pediatr. Dermatol.* **2018**, *35*, e224−e227.
(41) Oláh, A.; Tóth, B. I.; Borbíró, I.; Sugawara, K.; Szöllõsi, A. G.; Czifra, G.; Pál, B.; Ambrus, L.; Kloepper, J.; Camera, E.; Ludovici, M.; Picardo, M.; Voets, T.; Zouboulis, C. C.; Paus, R.; Bíró, T. Cannabidiol exerts sebostatic and antiinflammatory effects on human sebocytes. *J. Clin. Invest.* **2014**, *124*, 3713−3724.
(42) World Health Organization Technical Report Series 1013 1. Cannabidiol (CBD). Critical Review Report. Expert Committee on Drug Dependence. Fortieth Meeting. https://www.who.int/medicines/access/controlled-substances/CannabidiolCriticalReview.pdf (2018).
(43) Rambaran, T. F. Nanopolyphenols: A review of their encapsulation and anti-diabetic effects. *SN Appl. Sci.* **2020**, *2*, 1−26.
(44) Wang, L.; Wei, G.; Sun, L.; Liu, Z.; Song, Y.; Yang, T.; Sun, Y.; Guo, C.; Li, Z. Self-assembly of cinnamic acid-capped gold nanoparticles. *Nanotechnology* **2006**, *17*, 2907−2912.
(45) Schliebe, C.; Jiang, K.; Schulze, S.; Hietschold, H.; Cai, W.; Lang, H. A convenient light initiated synthesis of silver and gold nanoparticles using a single source precursor. *Chem. Commun.* **2013**, *49*, 3991−3993.
(46) Shaabani, E.; Amini, S. M.; Kharrazi, S.; Tajerian, R. Curcumin coated gold nanoparticles: synthesis, characterization, cytotoxicity, antioxidant activity and its comparison with citrate coated gold nanoparticles. *Nanomed. J.* **2017**, *4*, 115−125.
(47) Gupta, D.; Jamwal, D.; Rana, D.; Katoch, A. Microwave Synthesized Nanocomposites for Enhancing Oral Bioavailability of Drugs. In *Applications of Nanocomposite Materials in Drug Delivery*; Elsevier, 2018; pp 619−632.
(48) Kesavan Pillai, S.; Ray, S. S.; Scriba, M.; Bandyopadhyay, J.; Roux-van der Merwe, M. P.; Badenhorst, J. Microwave assisted green synthesis and characterization of silver/montmorillonite heterostructures with improved antimicrobial properties. *Appl. Clay Sci.* **2013**, *83−84*, 315−321.
(49) Dave Rutesh, H. Overview of Pharmaceutical Excipients used in Tablets and Capsules. *Drug Topics*, https://www.drugtopics.com/view/overview-pharmaceutical-excipients-used-tablets-and-capsules, (accessed 2020-10-28).
(50) Koczkur, K. M.; Mourdikoudis, S.; Polavarapu, L.; Skrabalak, S. E. Poly(vinyl pyrrolidone) in nanoparticle synthesis. *Dalt. Trans.* **2015**, *44*, 17883−17905.
(51) Chang, G.; Luo, Y.; Lu, W.; Liao, F.; Sun, X. Hydrothermal synthesis of ultra-highly concentrated, well-stable Ag nanoparticles and their application for enzymeless hydrogen peroxide detection. *J. Nanopart. Res.* **2011**, *13*, 2689−2695.
(52) Kuppusamy, P.; Yusoff, M. M.; Maniam, G. P.; Govindan, N. Biosynthesis of metallic nanoparticles using plant derivatives and their new avenues in pharmacological applications − An updated report. *Saudi Pharm. J.* **2016**, *24*, 473−484.
(53) Singh, P.; Pandit, S.; Garnæs, J.; Tunjic, S.; Mokkapati, V. R.; Sultan, A.; Thygesen, A.; Mackevica, A.; Mateiu, R. V.; Daugaard, A. E.; Baun, A.; Mijakovic, I. Green synthesis of gold and silver nanoparticles from cannabis sativa (Industrial hemp) and their capacity for biofilm inhibition. *Int. J. Nanomedicine* **2018**, *13*, 3571−3591.
(54) May, B. M. M.; Oluwafemi, O. S. Sugar-reduced gelatin-capped silver nanoparticles with high selectivity for colorimetric sensing of Hg 2+ and Fe 2+ ions in the midst of other metal ions in aqueous solutions. *Int. J. Electrochem. Sci.* **2016**, *11*, 8096−8108.
(55) Kumar, M.; Devi, P.; Kumar, A. Structural analysis of PVP capped silver nanoparticles synthesized at room temperature for optical, electrical and gas sensing properties. *J. Mater. Sci. Mater. Electron.* **2017**, *28*, 5014−5020.
(56) Liu, Y. S.; Chang, Y. C.; Chen, H. H. Silver nanoparticle biosynthesis by using phenolic acids in rice husk extract as reducing agents and dispersants. *J. Food Drug Anal.* **2018**, *26*, 649−656.
(57) Khan, M. A. M.; Kumar, S.; Ahamed, M.; Alrokayan, S. A.; AlSalhi, M. S. Structural and thermal studies of silver nanoparticles and electrical transport study of their thin films. *Nanoscale Res. Lett.* **2011**, *6*, 1−8.
(58) Ghosh, S.; Patil, S.; Ahire, M.; Kitture, R.; Gurav, D. D.; Jabgunde, A. M.; Kale, S.; Pardesi, K.; Shinde, V.; Bellare, J.; Dhavale, D. D.; Chopade, B. A. Gnidia glauca flower extract mediated synthesis of gold nanoparticles and evaluation of its chemocatalytic potential. *J. Nanobiotechnology* **2012**, *10*, No. 17.
(59) Pluchery, O.; Remita, H.; Schaming, D. Demonstrative experiments about gold nanoparticles and nanofilms: An introduction to nanoscience. *Gold Bull.* **2013**, *46*, 319−327.
(60) Devi, R. A.; Francis, A. P.; Devasena, T. Green-synthesized gold nanocubes functionalized with bisdemethoxycurcumin analog as an ideal anticancer candidate. *Green Process. Synth.* **2014**, *3*, 47−61.

https://doi.org/10.1021/acsomega.1c04303
ACS Omega 2021, 6, 29078−29090

(61) Dhumale, V. A.; Gangwar, R. K.; Datar, S. S.; Sharma, R. B. Reversible aggregation control of polyvinylpyrrolidone capped gold nanoparticles as a function of pH. *Mater. Express* **2012**, *2*, 311−318.
(62) Sett, A.; Gadewar, M.; Sharma, P.; Deka, M.; Bora, U. Green synthesis of gold nanoparticles using aqueous extract of Dillenia indica. *Adv. Nat. Sci. Nanosci. Nanotechnol.* **2016**, *7*, No. 025005.
(63) Mendoza-Cruz, R.; Parajuli, P.; Ojeda-Galvan, H. J.; Rodriguez, A. G.; Navarro-Contreras, H. R.; Velazquez-Salazar, J. J.; Bazan-Diaz, L.; Jose-Yacaman, M. Orthorhombic distortion in Au nanoparticles induced by high pressure. *CrystEngComm* **2019**, *21*, 3451−3459.
(64) Anker, J. N.; Hall, W. P.; Lyandres, O.; Shah, N. C.; Zhao, J.; Van Duyne, R. P. Biosensing with plasmonic nanosensors. *Nat. Mater.* **2008**, *7*, 442−453.
(65) Mayer, K. M.; Hafner, J. H. Localized surface plasmon resonance sensors. *Chem. Rev.* **2011**, *111*, 3828−3857.
(66) Petryayeva, E.; Krull, U. J. Localized surface plasmon resonance: Nanostructures, bioassays and biosensing-A review. *Anal. Chim. Acta.* **2011**, *706*, 8−24.
(67) Ashraf, J. M.; Ansari, M. A.; Khan, H. M.; Alzohairy, M. A.; Choi, I. Green synthesis of silver nanoparticles and characterization of their inhibitory effects on AGEs formation using biophysical techniques. *Sci. Rep.* **2016**, *6*, No. 20414.
(68) Rahman, A.; Kumar, S.; Bafana, A.; Dahoumane, S. A.; Jeffryes, C. Biosynthetic conversion of Ag+ to highly Stable Ag0 nanoparticles by wild type and cell wall deficient strains of chlamydomonas reinhardtii. *Molecules* **2018**, *24*, No. 98.
(69) Stevenson, A. P. Z.; Blanco Bea, D.; Civit, S.; Antoranz Contera, S.; Iglesias Cerveto, A.; Trigueros, S. Three strategies to stabilise nearly monodispersed silver nanoparticles in aqueous solution. *Nanoscale Res. Lett.* **2012**, *7*, No. 151.
(70) Introduction to Gold Nanoparticle Characterization | Cytodiagnostics Inc. https://www.cytodiagnostics.com/pages/introduction-to-gold-nanoparticle-characterization. (accessed 2020-10-19).
(71) Ogarev, V. A.; Rudoi, V. M.; Dement'eva, O. V. Gold Nanoparticles: Synthesis, optical properties, and application. *Inorg. Mater. Appl. Res.* **2018**, *9*, 134−140.
(72) Wriedt, T. Mie theory: A review. *Springer Ser. Opt. Sci.* **2012**, *169*, 53−71.
(73) Pawar, O.; Deshpande, N.; Dagade, S.; Waghmode, S.; Nigam Joshi, P. Green synthesis of silver nanoparticles from purple acid phosphatase apoenzyme isolated from a new source Limonia acidissima. *J. Exp. Nanosci.* **2016**, *11*, 28−37.
(74) Theivasanthi, T.; Alagar, M. Electrolytic synthesis and characterizations of silver nanopowder. *Nano Biomed. Eng.* **2012**, *4*, 58−65.
(75) Krishnamurthy, S.; Esterle, A.; Sharma, N. C.; Sahi, S. V. Yucca-derived synthesis of gold nanomaterial and their catalytic potential. *Nanoscale Res. Lett.* **2014**, *9*, No. 627.
(76) Biao, L.; Tan, S.; Meng, Q.; Gao, J.; Zhang, X.; Liu, Z.; Fu, Y. Green synthesis, characterization and application of proanthocyanidins-functionalized gold nanoparticles. *Nanomaterials* **2018**, *8*, No. 53.
(77) State, R.; Papa, F.; Munteanu, C.; Balint, I.; Ion, A.; Volceanou, A. Synthesis and characterization of poly(vinyl pyrrolidone) stabilized gold nanoparticles. *Rom. J. Mater.* **2015**, *45*, 262−266.
(78) Sahoo, P. K.; Kalyan Kamal, S.; Kumar, T.; Sreedhar, B.; Singh, A.; Srivastava, S. Synthesis of silver nanoparticles using facile wet chemical route. *Def. Sci. J.* **2009**, *59*, 447−455.
(79) Mohamed, T.; Matou-Nasri, S.; Farooq, A.; Whitehead, D.; Azzawi, M. Polyvinylpyrrolidone-coated gold nanoparticles inhibit endothelial cell viability, proliferation, and ERK1/2 phosphorylation and reduce the magnitude of endothelial-independent dilator responses in isolated aortic vessels. *Int. J. Nanomedicine* **2017**, *12*, 8813−8830.
(80) Brunning, A. Compound Interest - Analytical Chemistry − Infrared (IR) Spectroscopy. Compound Interest http://www.compoundchem.com/2015/02/05/irspectroscopy/ (accessed 2020-09-16).
(81) Weimer, J. J. Does the intensity of peaks in FTIR indicate interaction between two materials or not? https://www.researchgate.net/post/Does_the_intensity_of_peaks_in_FTIR_indicate_interaction_between_two_materials_or_not, (accessed 2020-10-20).
(82) Firoozi, S.; Jamzad, M.; Yari, M. Biologically synthesized silver nanoparticles by aqueous extract of Satureja intermedia C.A. Mey and the evaluation of total phenolic and flavonoid contents and antioxidant activity. *J. Nanostructure Chem.* **2016**, *6*, 357−364.
(83) Das, R. K.; Borthakur, B. B.; Bora, U. Green synthesis of gold nanoparticles using ethanolic leaf extract of *Centella asiatica*. *Mater. Lett.* **2010**, *64*, 1445−1447.
(84) Ligresti, A.; Moriello, A. S.; Starowicz, K.; Matias, I.; Pisanti, S.; De Petrocellis, L.; Laezza, C.; Portella, G.; Bifulco, M.; Di Marzo, V. Antitumor activity of plant cannabinoids with emphasis on the effect of cannabidiol on human breast carcinoma. *J. Pharmacol. Exp. Ther.* **2006**, *318*, 1375−1387.
(85) Casares, L.; García, V.; Garrido-Rodríguez, M.; Millán, E.; Collado, J. A.; García-Martín, A.; Peñarando, J.; Calzado, M. A.; de la Vega, L.; Muñoz, E. Cannabidiol induces antioxidant pathways in keratinocytes by targeting BACH1. *Redox Biol.* **2020**, *28*, No. 101321.
(86) Abotaleb, M.; Liskova, A.; Kubatka, P.; Büsselberg, D. Therapeutic potential of plant phenolic acids in the treatment of cancer. *Biomolecules* **2020**, *10*, 221.
(87) Lakshmipathy, M.; Nanda, A. Assessment of in vitro prophylactic efficacy of gallic acid fabricated silver nanoparticles. *J. Chem. Pharm. Res.* **2015**, *7*, 356−361.
(88) Nirmala, J. G.; Akila, S.; Nadar, M. S. A. M.; Narendhirakannan, R. T.; Chatterjee, S. Biosynthesized: *Vitis vinifera* seed gold nanoparticles induce apoptotic cell death in A431 skin cancer cells. *RSC Adv.* **2016**, *6*, 82205−82218.
(89) Zhao, Y.; Wang, Y.; Ran, F.; Cui, Y.; Liu, C.; Zhao, Q.; Gao, Y.; Wang, D.; Wang, S. A Comparison between sphere and rod nanoparticles regarding their in vivo biological behavior and pharmacokinetics. *Sci. Rep.* **2017**, *7*, No. 4131.
(90) Patel, H. M. Serum opsonins and liposomes: Their interaction and opsonophagocytosis. *Crit. Rev. Ther. Drug Carrier Syst.* **1992**, *9*, 39−90.
(91) Zein, R.; Sharrouf, W.; Selting, K. Physical properties of nanoparticles that result in improved cancer targeting. *J. Oncol.* **2020**, *2020*, 1−16.
(92) Maiorano, G.; Sabella, S.; Sorce, B.; Brunetti, V.; Malvindi, M. A.; Cingolani, R.; Pompa, P. P. Effects of cell culture media on the dynamic formation of protein-nanoparticle complexes and influence on the cellular response. *ACS Nano* **2010**, *4*, 7481−7491.
(93) Pal, A.; Shah, S.; Devi, S. Microwave-assisted synthesis of silver nanoparticles using ethanol as a reducing agent. *Mater. Chem. Phys.* **2009**, *114*, 530−532.

https://doi.org/10.1021/acsomega.1c04303
ACS Omega 2021, 6, 29078−29090